(Received 3 March 2025, Accepted 11 May 2025, Scheduled 18 May 2025)

# Design and Optimization of Fault Tolerant Dual-Permanent Magnet Excited Vernier Rim Driven Machine

Haibo Liao, Jingwei Zhu*, Yaqian Cai, Shukuan Zhang, and Kun Zang

*Marine Electrical Engineering College, Dalian Maritime University, Dalian 116026, China*

**ABSTRACT:** In order to improve the power density and torque density of the fault tolerant permanent magnet vernier rim driven machine, a new type of fault tolerant dual-permanent magnet excited vernier rim driven machine is proposed. Permanent magnets are placed on the stator and rotor of the machine, and more working harmonics are modulated by the dual-modulation effect of the air gap permeability by the teeth of the stator and rotor, thus improving the output performance of the machine. Aiming at the problem of more optimization parameters, a new optimization design method combining multi-objective genetic algorithm with single parameter scanning algorithm is proposed to optimize the design of machine. Compared with the traditional fault tolerant permanent magnet vernier rim driven machine, it is shown that the machine has better output performance.

## 1. INTRODUCTION

Magnetic field modulated permanent magnet machine is a hot research direction in recent years. This kind of machines can produce more effective harmonics at the expense of fundamental waves through magnetic field modulation and make multiple harmonics participate in electromagnetic energy conversion together. Thus, the torque output capacity of the machine can be improved [1].

Permanent Magnet Vernier Machine (PMVM) is widely used in various fields because of its low speed and high torque [2–5]. A design method of permanent magnet Vernier motor with low pole ratio is proposed in [6], which can realize high average torque and high-power factor at the same time. On this basis, the relationship among slot pole combination, modulation ratio, magnetic field modulation harmonic, and harmonic torque contribution is studied in [7], and a design method of multi-degree of freedom modulator is proposed. Two prototypes are manufactured to verify the feasibility of the design method. In order to improve the output performance of PMVM, a new Split Pole Permanent Magnet Vernier Machine (SP-PMVM) is proposed in [8]. The SP-PMVM with Halbach Permanent Magnet (PM) arrangement in the stator slot opening and consequent pole rotor is arranged which greatly improves the utilization rate of PM.

In [9], a PMVM using high-temperature superconducting materials is proposed to improve the electromagnetic performance of PMVMs at high polarity ratios. In [10], a variable flux PMVM with hybrid excitation was proposed, which improved the shortcomings of PMVM's poor speed regulation ability, and the multi-tooth splitter structure was used to effectively reduce the cogging torque of the machine.

The rim thruster is a new type of electric propulsion device which integrates machine body, propeller blade, and conduit. Due to the elimination of transmission shafting, mechanical seal, and machine cooling system, the power density and efficiency of ship propulsion system are significantly improved, and the operating noise is reduced [11]. For example, British Rolls-Royce [12], Norway Brunvoll, and other companies have realized the production of high-power rim thrusters.

At present, the integrated machines in the rim thruster are mainly brushless DC machine and PMSM. Brushless DC machine has the disadvantage of large output torque ripple. Although PMSM overcomes the disadvantage of large torque ripple, the power density is not high, and the production cost and underwater maintenance of equipment also restrict the further development of the rim thruster [13]. Therefore, Fault Tolerant Permanent Magnet Vernier Machine (FTPMVM) is applied to the rim thruster device in [14] to improve the ship propulsion efficiency and reliability. However, the problems of PMVM such as magnetic flux leakage between poles and large amount of PM also limit the application of FTPMVM in rim thruster [15–21].

In order to improve the output performance of Fault Tolerant Permanent Magnet Vernier Rim Driven Machine (FTPMV-RDM), this paper proposes a structure of Fault Tolerant Dual-Permanent Magnet Excited Vernier Rim Driven Machine (FTDPMEV-RDM). On the basis of the rotor excitation structure of FTPMV-RDM, FTDPMEV-RDM introduces a stator excitation structure and uses alternating poles and a magnetic concentrating structure at the same time, which not only reduces the amount of PM but also improves the output performance of the machine.

## 2. MACHINE TOPOLOGY AND THEORETICAL ANALYSIS

### 2.1. Machine Topology

The FTDPMEV-RDM structure, as shown in Fig. 1, is composed of a stator and a rotor, and the propeller is welded di-

* Corresponding author: Jingwei Zhu (zjwdl@dlmu.edu.cn).

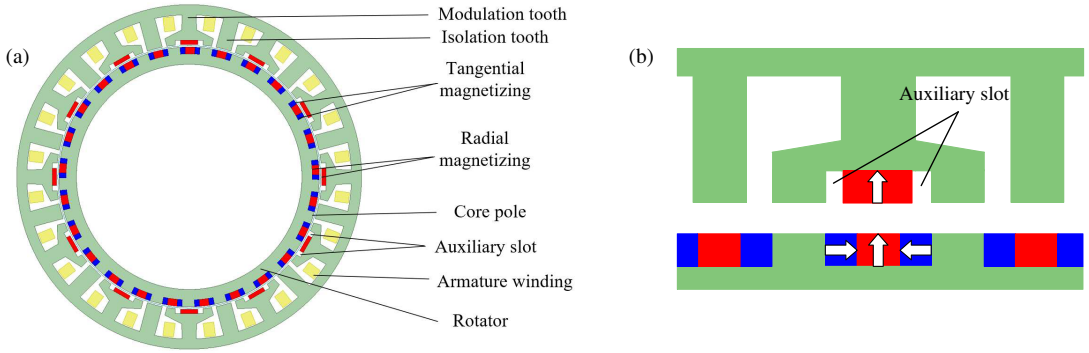


**FIGURE 1**. Topological structure of machine and magnetization direction of PM. (a) Topological structure of machine. (b) Magnetization direction of PM.

rectly to the inner surface of the rotor with non-conductive materials. The stator part is alternately arranged by armature teeth and isolation tooth and is unevenly distributed. Two modulation poles are opened at the end of the armature teeth to form an isolation slot. Each isolation tooth is seen as a modulation pole, and all the modulation poles modulate the air gap magnetic field together. The stator permanent magnet is arranged at the isolation slot, and the two sides of the permanent magnet are slotted to form an auxiliary slot. The alternating pole structure is adopted in the rotor part. In order to improve the output torque of the machine, Halbach array is introduced, and each of the three PMs is a group. The middle PM is magnetized in radial direction, and the PM on both sides are magnetized in tangential direction.

The stator of FTDPMEV-RDM adopts six-phase single-layer centralized winding. There is only one set of winding in each slot, and the winding is only wound on the armature teeth. This winding form can realize the physical isolation between the phase windings and avoid the inter-phase short-circuit fault. At the same time, each phase is driven by a separate H-bridge inverter circuit to achieve electrical isolation. Moreover, the existence of isolation tooth reduces the mutual inductance between windings and improves the fault tolerance of FTDPMEV-RDM.

The working principle of FTDPMEV-RDM is based on the modulation effect of bidirectional magnetic field. In order to generate a stable torque, the following relationships need to be met:

$$\begin{aligned} P_a &= |iP_{rm} \pm jN_s| = |iP_{sm} \pm jN_r| \\ & i = 1, 3, 5...; \quad j = 0, 1, 2... \end{aligned} \tag{1}$$

where $P_a$ is the equivalent pole pair number of armature winding, $P_{rm}$ the pole pair number of rotor PMs, $P_{sm}$ the pole pair number of stator PMs, $N_s$ the number of stator magnetic conductance periods, and $N_r$ the number of rotor magnetic conductance cycles.

### 2.2. Theoretical Analysis

FTDPMEV-RDM is a magnetic field modulated permanent magnet machine. The PM on the stator and rotor will generate PM magnetic field in the air gap and be modulated by the corresponding rotor and the modulation teeth on the stator. The modulation will produce abundant harmonics in the air gap, in which the effective working harmonics interact with the magnetic field harmonics generated by the armature windings to produce stable torque.

To simplify the analysis, FTDPMEV-RDM can be regarded as two independent parts. The first part is composed of stator PM, rotor tooth, and armature winding, which is excited only by stator PM, as shown in Fig. 2(a); the second part is composed of rotor PM, stator tooth, and armature winding, which is excited only by rotor PM, as shown in Fig. 2(b).

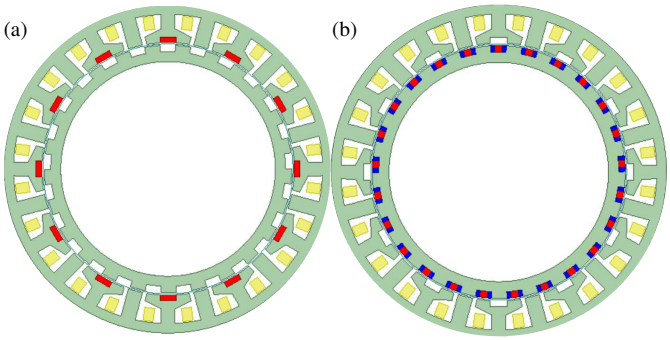


**FIGURE 2**. FTDPMEV-RDM structure under different excitation conditions, (a) stator PM excitation only, (b) rotor PM excitation only.

When the FTDPMEV-RDM is excited only by the stator PM, the magnetomotive force (MMF) generated by the stator PM in the air gap is:

$$F_s(\theta) = \sum_{n=1,3,5...}^{\infty} F_{sn} \cos\left(nP_{sm}\theta\right) \tag{2}$$

where $F_{sn}$ is the Fourier coefficient of the stator MMF, and $n$ is the number of harmonics.

Because the salient pole rotor structure is adopted in FTDPMEV-RDM, the air gap magnetic conductance distribution in the circumferential direction is uneven. It can be simplified to the rotor magnetic conductance model shown in Fig. 3. Then the Fourier expression of the air gap magnetic

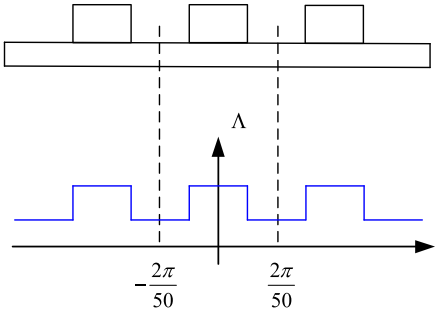


**FIGURE 3**. Rotor magnetic conductance model.

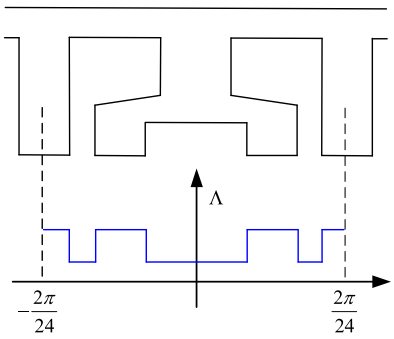


**FIGURE 4**. Stator magnetic conductance model.

conductance of the rotor slot is:

$$\Lambda_r(\theta,t) = \Lambda_0 + \sum_{m=1,2,3\ldots}^{\infty} \Lambda_{rm}\cos[mN_r(\theta-\omega_r t-\theta_0)] \quad (3)$$

where $\Lambda_0$ is the DC component of rotor conductance, $\Lambda_{rm}$ the Fourier coefficient of rotor conductance, $m$ the number of harmonics, $\omega_r$ the radial rotation speed of rotor, and $\theta_0$ the initial position of rotor.

Therefore, the air gap flux density produced by the stator PM is:

$$\begin{aligned} B_s(\theta,t) &= F_s(\theta)\Lambda_r(\theta,t) = \sum_{n=1,3,5\ldots}^{\infty} F_{sn}\Lambda_0\cos(nP_{sm}\theta) \\ &+\frac{1}{2}\sum_{n=1,3,5\ldots}^{\infty}\sum_{m=1,2,3\ldots}^{\infty} F_{sn}\Lambda_{rm}\cos\mu \\ &+\frac{1}{2}\sum_{n=1,3,5\ldots}^{\infty}\sum_{m=1,2,3\ldots}^{\infty} F_{sn}\Lambda_{rm}\cos\nu \end{aligned} \quad (4)$$

where:

$$\begin{aligned} \mu &= (nP_{sm}+mN_r)\theta - mN_r(\omega_r t+\theta_0) \\ \nu &= (nP_{sm}-mN_r)\theta + mN_r(\omega_r t+\theta_0) \end{aligned}$$

In order to simplify the analysis, the alternating pole of the magnetic concentration structure is regarded as the conventional alternating pole structure. When the FTDPMEV-RDM is excited only by the rotor PM, the MMF generated by the PM in the air gap is:

$$F_r(\theta,t) = \sum_{n=1,3,5\ldots}^{\infty} F_{rn}\cos[nP_{rm}(\theta-\omega t-\varphi)] \quad (5)$$

where $F_{rn}$ is the Fourier coefficient of the rotor MMF, and $\varphi$ is the initial angle of the stator.

Considering the uneven distribution of the stator armature teeth and isolation teeth on the circumference, the stator magnetic conductance model is shown in Fig. 4. Then, the expression of stator conductance is:

$$\Lambda_s(\theta) = \Lambda_1 + \sum_{m=1,2,3\ldots}^{\infty} \Lambda_{sm}\cos(mN_s\theta) \quad (6)$$

where $\Lambda_1$ is the DC component of the stator conductance, and $\Lambda_{sm}$ is the Fourier coefficient of the stator conductance.

Therefore, the air gap flux density produced by the rotor PM is:

$$\begin{aligned} B_r(\theta,t) &= F_r(\theta)\Lambda_s(\theta,t) = \sum_{n=1,3,5\ldots}^{\infty} F_{rn}\Lambda_1\cos\beta_1 \\ &+\frac{1}{2}\sum_{n=1,3,5\ldots}^{\infty}\sum_{m=1,2,3\ldots}^{\infty} F_{rn}\Lambda_{sm}\cos\beta_2 \\ &+\frac{1}{2}\sum_{n=1,3,5\ldots}^{\infty}\sum_{m=1,2,3\ldots}^{\infty} F_{rn}\Lambda_{sm}\cos\beta_3 \end{aligned} \quad (7)$$

where:

$$\begin{aligned} \beta_1 &= nP_{rm}(\theta-\omega t-\varphi) \\ \beta_2 &= (nP_{rm}+mN_s)\theta - mP_{rm}(\omega_r t+\varphi) \\ \beta_3 &= (nP_{rm}-mN_s)\theta - mP_{rm}(\omega_r t+\varphi) \end{aligned}$$

From Equation (4) and Equation (7), the working harmonics of FTPMV-RDM under two separate excitation modes can be obtained, as shown in Table 1.

**TABLE 1**. The operating harmonics generated by the two excitation methods.

| | Stator excitation | Rotor excitation |
|---|---|---|
| Part I | $nP_{sm}$ | $nP_{rm}$ |
| Part II | $\lvert nP_{sm}+mN_r\rvert$ | $\lvert nP_{rm}+mN_s\rvert$ |
| Part III | $\lvert nP_{sm}-mN_r\rvert$ | $\lvert nP_{rm}-mN_s\rvert$ |

The excitation mode of FTDPMEV-RDM is the superposition of the two excitation methods. As can be seen from Table 1, the FTDPMEV-RDM with stator and rotor co-excitation has more operating harmonics than the single-excitation FTPMV-RDM.

## 3. FINITE ELEMENT SIMULATION ANALYSIS

In order to verify the correctness of the above theoretical analysis, this section will analyze the electromagnetic performance of FTDPMEV-RDM through the finite element software. The

**TABLE 2.** FTDPMEV-RDM initial parameters.

| Items | Values | Items | Values |
|---|---|---|---|
| Number of phases | 6 | Number of slots | 24 |
| Pole logarithm of PM | 25 | Axial length (mm) | 45 |
| Stator outer diameter (mm) | 260 | Stator inner diameter (mm) | 200 |
| Rotor outer diameter (mm) | 196 | Rotor inner diameter (mm) | 170 |
| Pole arc coefficient | 0.5 | Rotor PM height (mm) | 5 |
| Stator PM width (mm) | 13 | Stator PM thickness (mm) | 4.5 |
| Auxiliary slot width (mm) | 1 | Auxiliary slot depth (mm) | 4.5 |

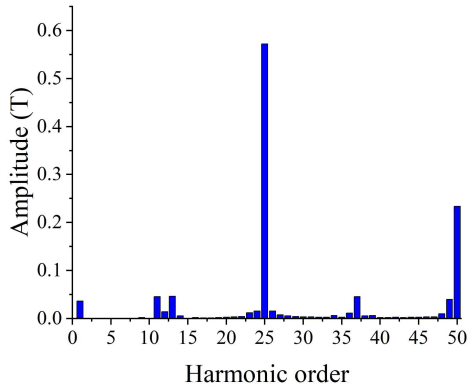


**FIGURE 5.** Harmonic spectrum of air gap flux density when only rotor PM is excited.

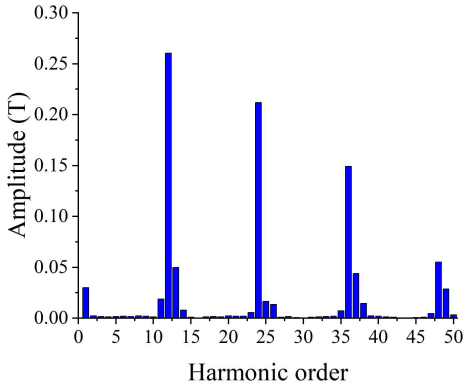


**FIGURE 6.** Harmonic spectrum of air gap flux density when only stator PM is excited.

initial configuration parameters of FTDPMEV-RDM are shown in Table 2.

### 3.1. Magnetic Density Analysis of No-Load Air Gap

Figure 5 shows the harmonic spectrum of the air gap flux density when only the PM excitation of the rotor is considered. It can be seen that in addition to the harmonics generated by the PMs, the air gap magnetic density harmonics also produce harmonics such as 1st, 11th, 13th, and 37th ones. Fig. 6 shows the harmonic spectrum of the air gap flux density when only the PM excitation of the stator is considered. It can be seen that in addition to the harmonics generated by PMs, the 1st, 13th, and 37th harmonics generated by modulation also have higher amplitudes. Through the comparison between the theoretical analysis and simulation results, it can be seen that the magnetic field modulation process of FTDPMEV-RDM is completely consistent with the bi-directional magnetic field modulation theory.

Figure 7 compares the air gap flux density of stator and rotor PMs with that of stator and rotor PMs alone. It can be seen from Fig. 7 that the air gap magnetic density distributions obtained by the two methods are almost the same, so the analysis of the bi-directional magnetic field modulation effect of FTDPMEV-RDM can be equivalent by the superposition of the single PM magnetic field.

Figure 8 shows the harmonic spectrum of air gap flux density acting alone by PM and its superposition result. It can be seen from the Fig. 8 that after bi-directional magnetic field modulation, the amplitudes of these main working harmonics obtained

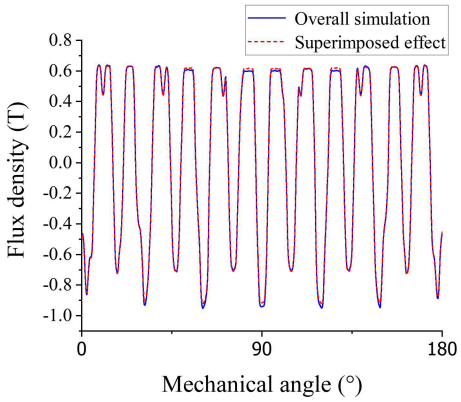


**FIGURE 7.** Air gap flux density when stator and rotor PMs act together.

by superposition are obviously larger than those of air-gap magnetic density harmonics excited by PMs alone.

### 3.2. Analysis of No-Load Back EMF

Figure 9 shows the no-load back EMF waveform. It can be seen from Fig. 9 that when only the stator PM and rotor PM are excited separately, the effective values of the no-load back EMF are 20.387 V and 101.917 V, respectively. When the stator PM and rotor PM are excited at the same time, the no-load back EMF is 119.907 V, which is approximately equal to the sum of the separate excitation of the stator PM and rotor PM. It shows that FTDPMEV-RDM makes use of the bi-directional modulation of air gap flux density, so that the PMs with different pole pairs on the stator and rotor can effectively couple the magnetic field on the armature winding.

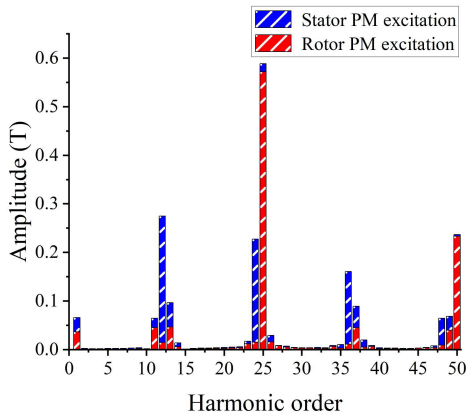


**FIGURE 8**. Superposition diagram of air gap flux density harmonics when stator and rotor PM act alone.

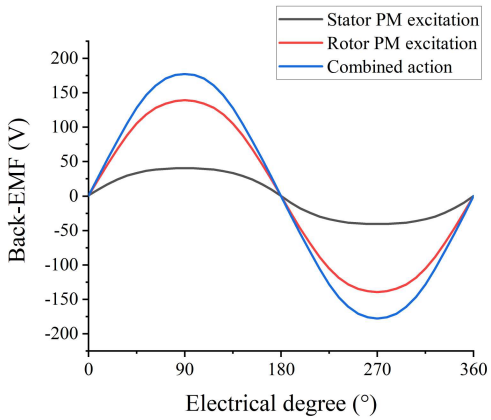


**FIGURE 9**. No-load back EMF waveform.

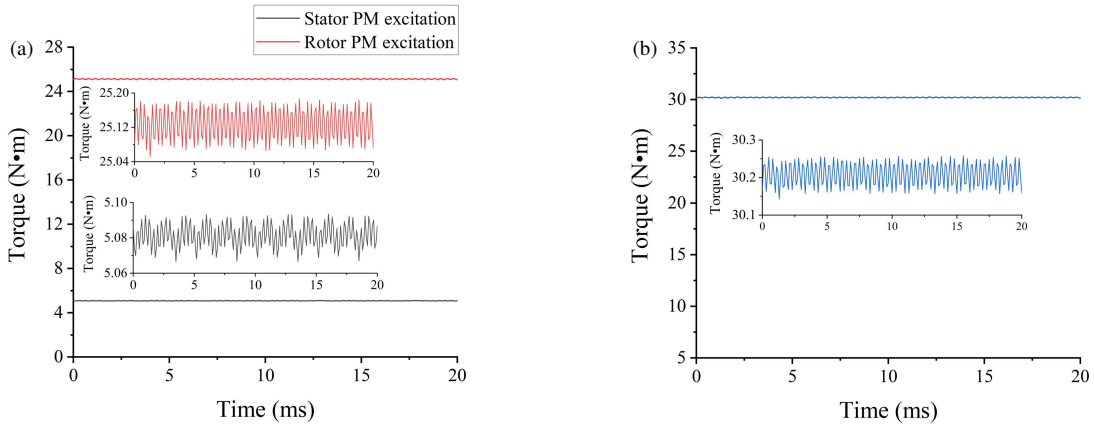


**FIGURE 10**. Electromagnetic torque waveform. (a) Stator PM or rotor PM excitation only. (b) The stator and rotor PM are co-excited.

### 3.3. Electromagnetic Torque Analysis

Figure 10 shows the electromagnetic torque waveform of FTDPMEV-RDM. It can be seen from Fig. 10 that when only the stator PM and rotor PM are excited separately, the average electromagnetic torque is 5.081 N·m and 25.126 N·m, respectively. When the stator PM and rotor PM are excited at the same time, the average electromagnetic torque is 30.255 N·m, which is approximately equal to the sum of the separate excitation of the stator PM and rotor PM. The results show that the air gap magnetic field of FTDPMEV-RDM has a good bi-directional modulation effect and can effectively improve the electromagnetic torque of the machine.

## 4. OPTIMAL DESIGN OF MACHINE STRUCTURE

### 4.1. Optimization Parameters and Selection of Optimization Objectives

Select the following six structural parameters, namely polar arc coefficient $\alpha$, rotor PM height $h_r$, stator PM thickness $h_s$, stator PM width $f_s$, auxiliary slot width $f$, and slot opening width $b_{s0}$, as the optimization variables of FTDPMEV-RDM. The maximum average output torque and minimum torque ripple are selected as the optimization objectives of FTDPMEV-RDM. The optimized structural parameters are shown in Fig. 11, and the values of the optimized parameter range are shown in Table 3.

**TABLE 3**. Range of optimization parameter.

| Items | Lower limit | Upper limit |
|---|---|---|
| Polar arc coefficient $\alpha$ | 0.4 | 0.7 |
| Rotor PM height $h_r$/mm | 4 | 8 |
| Stator PM thickness $h_s$/mm | 3 | 5 |
| Stator PM width $f_s$/mm | 11 | 15 |
| Auxiliary slot width $f$/mm | 1 | 4 |
| Slot opening width $b_{s0}$/mm | 2.5 | 4.5 |

The polar arc coefficient in the alternating pole structure is defined as follows:

$$\alpha = \frac{l_{pm}}{\tau} \tag{8}$$

$$\tau = l_{pm} + l_{Fe} \tag{9}$$

where $l_{pm}$ is the arc length of the PM, and $l_{Fe}$ is the arc length of the core pole.

Torque ripple is defined as follows:

$$T_r = \frac{T_{pk2pk}}{T_{avg}} = \frac{T_{\max} - T_{\min}}{T_{avg}} \tag{10}$$

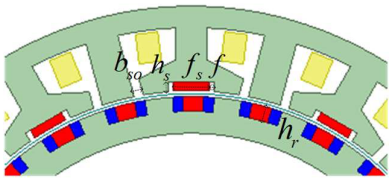


**FIGURE 11**. Optimizing structural parameters.

where $T_{pk2pk}$ is the output torque peak, and $T_{avg}$ is the average torque.

### 4.2. Optimization Design Method

FTDPMEV-RDM has many stator and rotor parameters, and the coupling between parameters is more complex. If the traditional single-parameter scanning method is used for optimization, it will produce a large number of simulation points, and the optimization efficiency is low. Therefore, this paper designs an optimization method of classified design according to the sensitivity level. The design method of multi-objective optimization is adopted for the optimization parameters with high sensitivity. The single parameter scanning method is used to optimize the low sensitivity parameters. The optimized design process is shown in Fig. 12.

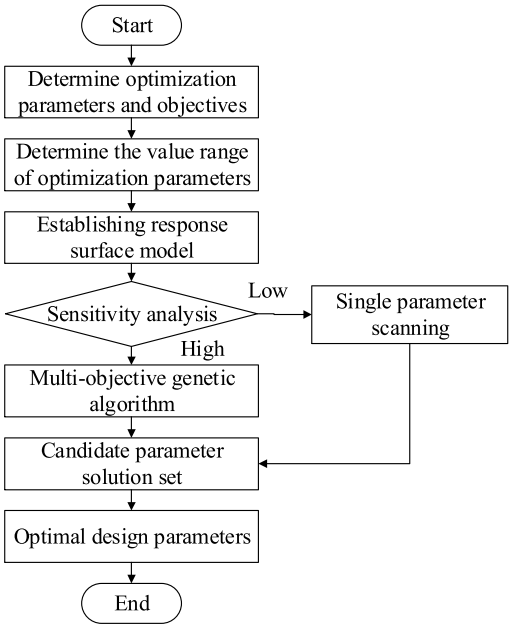


**FIGURE 12**. Optimization flowchart.

The sensitivity index of FTDPMEV-RDM optimization parameters to two key optimization objectives can be expressed as follows:

$$S_j(x_i) = \frac{V(E(y_j/x_i))}{V(y_j)} \quad (i = 1, 2, ...6)\ (j = 1, 2) \quad (11)$$

where $x_i$ represents the $i$th design variable, $y_i$ the $j$th optimization goal, $E(y_i|x_i)$ the average value when $x_i$ is constant, $V(E(y_i|x_i))$ the variance of $E(y_i|x_i)$, and $V(y_i)$ the variance of $y_i$. $S_j(x_i)$ is the sensitivity index of the $i$th design variable

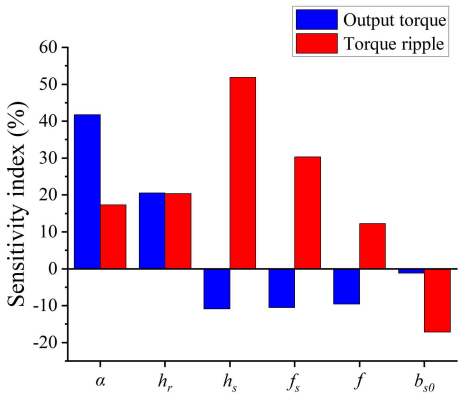


**FIGURE 13**. Sensitivity index of FTDPMEV-RDM optimization parameters.

to the $j$th optimization objective. Fig. 13 shows the sensitivity index of each parameter.

According to the results of sensitivity analysis, the ranking of the optimization parameters can be obtained in Fig. 14.

| Average torque sensitivity | | Torque ripple sensitivity |
|---|---|---|
| $\alpha$ | High | $h_s$ |
| $h_r$ | | $f_s$ |
| $h_s$ | | $h_r$ |
| $f_s$ | | $\alpha$ |
| $f$ | | $b_{s0}$ |
| $b_{s0}$ | Low | $f$ |

**FIGURE 14**. Sensitivity sequencing of optimized parameters.

It can be seen from Fig. 14 that the polar arc coefficient $\alpha$, rotor PM height $h_r$, stator PM thickness $h_s$, and stator PM width $f_s$ have high sensitivity response to the average torque and torque ripple of FTDPMEV-RDM. Therefore, these four parameters are selected to establish the corresponding Kriging model, and multi-objective genetic algorithm is used to optimize the design. For the auxiliary slot width $f$ and slot opening width $b_{s0}$, the sensitivity response to the average torque and torque ripple of FTDPMEV-RDM is low, so the single parameter scanning method is used to optimize the design.

### 4.3. Optimization Scheme Implementation

The Kriging response surface model of FTDPMEV-RDM is established under four parameters: polar arc coefficient $\alpha$, rotor PM height $h_r$, stator PM thickness $h_s$, and stator PM width $f_s$ as shown in Figs. 15 and 16.

Multi-objective genetic algorithm (MOGA) is used for the above four optimization parameters. The single parameter scanning method is used for the remaining two parameters, as shown in Fig. 17.

On the basis of the above experimental data, the multi-objective genetic algorithm and single parameter scanning

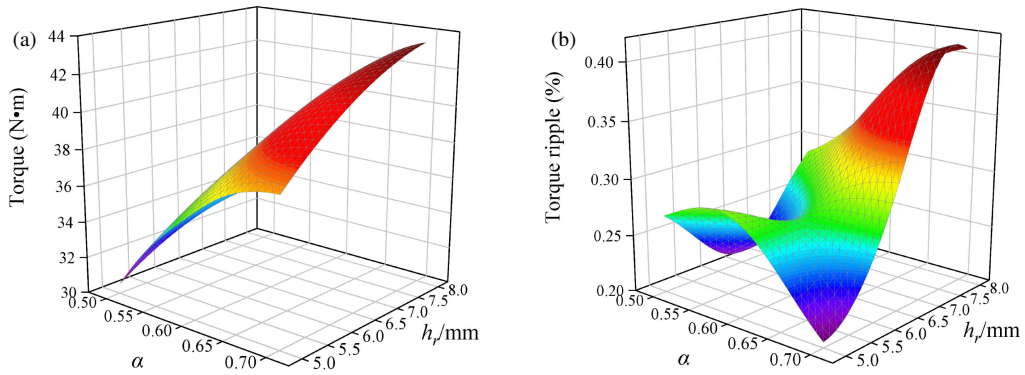


**FIGURE 15**. $\alpha$ and $h_r$ the kriging model. (a) Kriging model of average torque with respect to $\alpha$ and $h_r$. (b) Kriging model of torque ripple with respect to $\alpha$ and $h_r$.

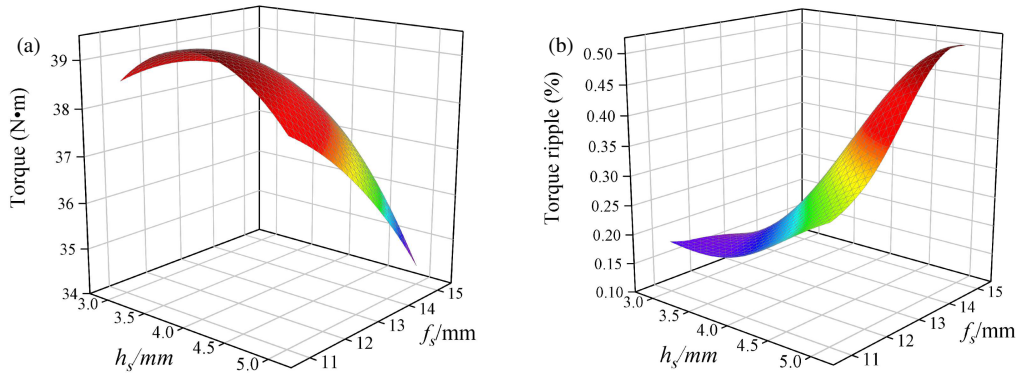


**FIGURE 16**. $h_s$ and $f_s$ the Kriging model. (a) Kriging model of average torque with respect to $h_s$ and $f_s$. (b) Kriging model of torque ripple with respect to $h_s$ and $f_s$.

**TABLE 4**. Machine parameters of initial and optimized.

| Items | Initial | Optimized |
|---|---|---|
| Polar arc coefficient $\alpha$ | 0.5 | 0.6 |
| Rotor PM height $h_r$/mm | 5 | 5.2 |
| Stator PM thickness $h_s$/mm | 4.5 | 3 |
| Stator PM width $f_s$/mm | 13 | 12.6 |
| Auxiliary slot width $f$/mm | 1 | 2 |
| Auxiliary slot width $f$/mm | 3.5 | 3.2 |
| Torque/Nm | 30.35 | 36.29 |
| Torque ripple/% | 0.30 | 0.24 |

method are combined to get the optimal parameters of the machine as shown in Table 4.

It can be calculated from Table 4 that after the optimization design of FTDPMEV-RDM, the average output torque of the machine increases from 30.35 N·m to 36.29 N·m, an increase of 19.6%. The torque ripple decreases from 0.30% to 0.24%, a decrease of 20%. It is proved that the optimization method proposed in this paper is efficient.

## 5. PERFORMANCE COMPARISON

The main purpose of this section is to compare and analyze the electromagnetic performances of FTDPMEV-RDM and FTPMV-RDM. In order to ensure the fairness of the comparison, the main size, turn number of windings per phase, current density, and winding type are kept the same. Because the excitation modes of the two kinds of machines are different, the polar arc coefficient of FTDPMEV-RDM is set to 0.6, and the amount of permanent magnet is 104.6 mm$^3$. The polar arc coefficient of FTPMV-RDM is 0.8, and the amount of permanent magnet is 112.2 mm$^3$. Because the propeller is a non-magnetic conductive material, it is not taken into account in the model.

### 5.1. Comparison of Magnetic Density Performance of No-Load Air Gap

The no-load air gap flux density and its harmonic analysis of the two kinds of machines are shown in Fig. 18. It can be seen from Fig. 18 that the no-load air gap magnetic density of FTDPMEVRDM is slightly higher than that of FTPMV-RDM. From the Fourier analysis, it can be seen that the magnetic density of FTDPMEV-RDM is slightly lower than that of FTPMV-RDM at the 25th harmonic. However, FTDPMEV-RDM can modulate more working harmonics than FTPMV-RDM, thus improving the output energy force of the machine.

### 5.2. Performance Comparison of No-Load Back EMF

The comparison of the no-load back EMF of the two machines is shown in Fig. 19. Through the calculation, the no-load back

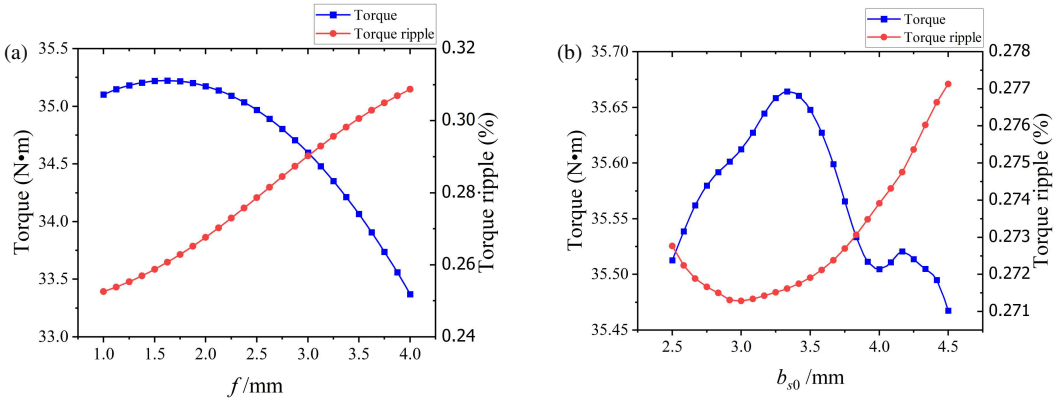


**FIGURE 17**. Single parameter scan result. (a) $f$ on average torque and torque ripple. (b) $b_s$ on average torque and torque ripple.

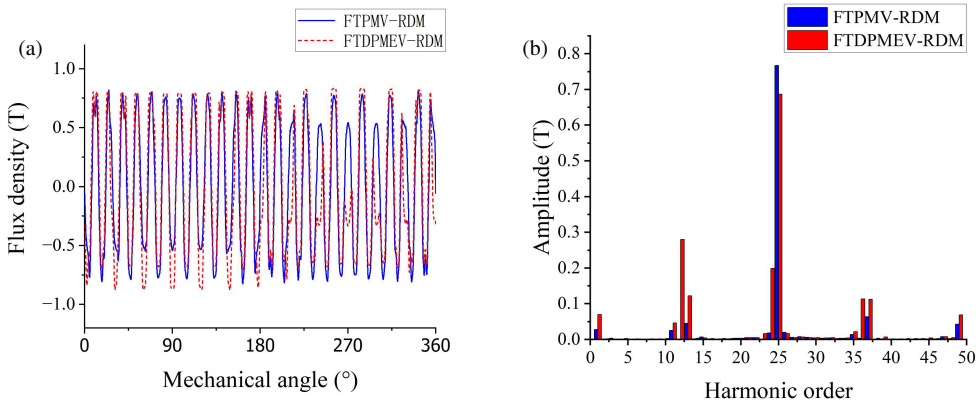


**FIGURE 18**. Magnetic density of no-load air gap. (a) No-load air-gap magnetic density waveform. (b) Harmonic spectrum analysis.

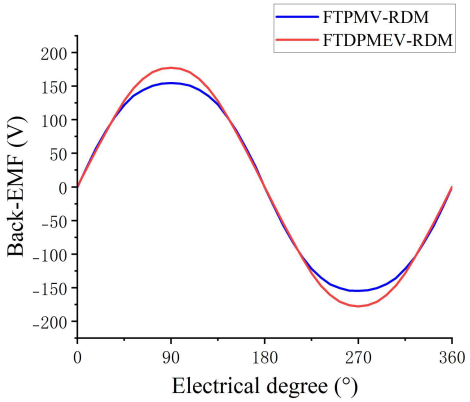


**FIGURE 19**. Comparison of no-load back-EMF.

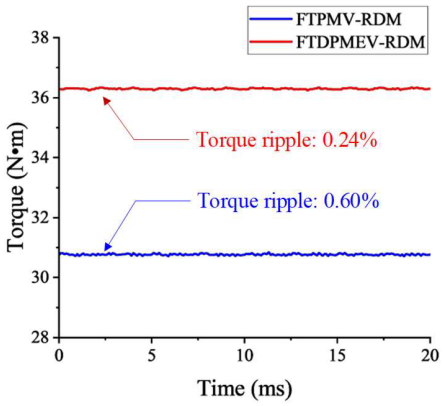


**FIGURE 20**. Output torque performance comparison.

EMF of FTDPMEV-RDM is 127 V, which is 9.4% higher than that of FTPMV-RDM. In addition, the harmonic distortion rate of FTDPMEV-RDM is 0.7%, which is much lower than 5.3% of FTPMV-RDM. It shows that FTDPMEV-RDM has higher sinusoidal property.

### 5.3. Torque Performance Comparison

When the phase current is 2.8 A, the output torques of the two machines are compared as shown in Fig. 20. The average output torques of FTDPMEV-RDM and FTPMV-RDM are 36.29 N·m and 30.75 N·m, respectively. The average output torque of FTDPMEV-RDM is 18% higher than that of FTPMV-RDM when the amount of PM is reduced by 7%, and the torque ripple decreases by 60%. Therefore, the new machine topology proposed in this paper has higher torque density.

### 5.4. Fault-Tolerant Performance Comparison

Taking phase A as an example, the self-inductance and mutual inductance of the two machines are shown in Table 5. The self-inductance effective value of FTDPMEV-RDM is 40.6 mH, and

**TABLE 5**. Self-inductance and mutual inductance.

| | FTPMV-RDM | FTDPMEV-RDM |
|---|---|---|
| $L_{AA}$/mH | 28.4695 | 40.6232 |
| $L_{AB}$/mH | 0.0648 | 0.1129 |
| $L_{AC}$/mH | 0.0647 | 0.1128 |
| $L_{AU}$/mH | 0.2386 | 0.3288 |
| $L_{AV}$/mH | 0.2386 | 0.3286 |
| $L_{AW}$/mH | 0.0055 | 0.0477 |

the coupling coefficient is 0.81%. The self-inductance effective value of FTPMVRDM is 28.5 mH, and the coupling coefficient is 0.83%. FTDPMEV-RDM has larger self-inductance and smaller coupling coefficient, which indicates that it has stronger power to restrain short-circuit current and better fault tolerance.

### 5.5. Efficiency and Coe loss

The efficiency and core iron loss of the two machines are shown in Fig. 21. It can be seen from the figure that the core loss of FTDPMEV-RDM is higher, because the machine has more working harmonics, so the core loss is higher. But the efficiencies of the two machine are not much different. And FTDPMEV-RDM has higher output torque, so FTDPMEV-RDM has better output performance.

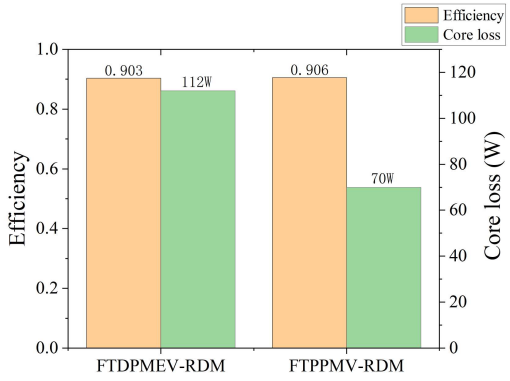


**FIGURE 21**. Efficiency and core loss.

## 6. CONCLUSION

In order to improve the output performance of FTPMV-RDM, a new FTDPMEV-RDM is proposed in this paper. Through theoretical and simulation analysis, the feasibility of the new topology is proved. In order to solve the problems of many optimization parameters and large amount of calculation of motor, a new optimization method based on sensitivity layering is proposed to optimize the motor. Finally, the output performances of FTDPMEV-RDM and FTPMV-RDM under the optimal structure are compared, which proves the superiority of the FTDPMEV-RDM proposed in this paper. Because FTDPMEV-RDM adopts bilateral excitation structure, its working harmonics are more, which leads to large core loss. Therefore, other scholars can optimize the design of FTDPMEV-RDM from the aspect of reducing core loss.

## ACKNOWLEDGEMENT

This work was supported in part by the National Natural Science Foundation of China under Grant 52377037, in part by the Fundamental Research Funds for the Central Universities of China under Grant 3132023522.

## REFERENCES

[1] Lin, H., Y. Zhang, H. Yang, *et al.*, "Research status and latest progress of permanent magnet vernier motors," *China Journal of Electrical Engineering*, Vol. 36, No. 18, 5021–5034, 2016.

[2] Du, Z. S. and T. A. Lipo, "Design of an improved dual-stator ferrite magnet vernier machine to replace an industrial rare-earth IPM machine," *IEEE Transactions on Energy Conversion*, Vol. 34, No. 4, 2062–2069, Dec. 2019.

[3] Wu, D., Z. Xiang, X. Zhu, L. Quan, M. Jiang, and Y. Liu, "Optimization design of power factor for an in-wheel vernier PM machine from the perspective of air-gap harmonic modulation," *IEEE Transactions on Industrial Electronics*, Vol. 68, No. 10, 9265–9276, Oct. 2021.

[4] Qiao, T., J. Zhu, and X. Wang, "Performance comparison of spoke array fault tolerant PM vernier rim driven machine with different numbers of flux modulation poles," *Progress In Electromagnetics Research M*, Vol. 105, 55–65, 2021.

[5] Ling, Z., Q. Zhang, and M. Xu, "Design and analysis of linear primary permanent magnet vernier machines with different winding configurations," *Progress In Electromagnetics Research C*, Vol. 151, 33–43, 2024.

[6] Zhao, Y., D. Li, X. Ren, Z. Liang, and R. Qu, "Low pole-pair ratio integration design of permanent magnet vernier machine with improved power factor," *IEEE Transactions on Industrial Electronics*, Vol. 71, No. 3, 2820–2830, Mar. 2024.

[7] Wang, R., B. Wang, D. Tian, H. Cai, M. Cheng, and W. Hua, "Slot pole combination analysis of FSCW-PMVM on magnetic field modulation performance," *IEEE Transactions on Transportation Electrification*, Vol. 11, No. 2, 5665–5675, Oct. 2024.

[8] Khan, S., F. Khan, W. Ullah, Z. Ahmad, and B. Ullah, "Split pole permanent magnet vernier machine with Halbach array magnets in stator slot opening and consequent pole rotor," *IEEE Access*, Vol. 10, 75 672–75 679, 2022.

[9] Kui, Z., L. Jing, Z. Min, and K. Yang, "Design and analysis of a novel U-PM vernier machine with HTS bulks," *Progress In Electromagnetics Research C*, Vol. 128, 97–111, 2022.

[10] Zhang, Y., J. Luo, M. Huang, Q. Huang, and D. Decker, "Design and experimental verification of variable flux permanent magnet vernier machine using time-stepping finite element method," *Progress In Electromagnetics Research C*, Vol. 129, 115–126, 2023.

[11] Li, Q., S. Abdullah, and M. R. M. Rasani, "A review of progress and hydrodynamic design of integrated motor pump-jet propulsion," *Applied Sciences*, Vol. 12, No. 8, 3824, Apr. 2022.

[12] Cai, B., Q. Xu, B. Tian, L. Qiu, W. Chai, J. Qi, and L. He, "Improvement of the efficiency for rim-driven thrusters through acceleration of gap flow," *Ocean Engineering*, Vol. 291, 116480, 2024.

[13] Ouyang, W., Z. Zhang, B. Liu, *et al.*, "Research status and development trend of ship flange thruster key technology," *Ship Engineering*, Vol. 46, No. 9, 14–32, 2024.

[14] Qiao, T., J. Zhu, and X. Wang, "Design and optimization of a flux-modulated fault-tolerant permanent magnet rim-driven machine with combined stator to improve torque density," *IEEE Transactions on Energy Conversion*, Vol. 38, No. 1, 75–88, 2023.

[15] Gao, Y., T. Kosaka, Y. Liu, M. Doppelbauer, and R. Qu, "Comparative analysis of double flux modulation permanent magnet machines with different stator PM arrangements," *IEEE Transactions on Industry Applications*, Vol. 58, No. 2, 1941–1951, Mar.–Apr. 2022.

[16] He, W., J. Zhu, Z. Wang, J. Yue, and T. Zhao, "Optimization of flux-concentrating consequent-pole permanent magnet fault tolerant vernier rim-driven motor," *Progress In Electromagnetics Research C*, Vol. 135, 241–253, 2023.

[17] Du, K., L. Xu, W. Zhao, and G. Liu, "Analysis and design of a fault-tolerant permanent magnet vernier machine with improved power factor," *IEEE Transactions on Industrial Electronics*, Vol. 69, No. 5, 4353–4363, May 2022.

[18] Bai, J., J. Liu, G. Liu, Y. Liu, and P. Zheng, "Investigation of the power factor of magnetic-field modulated brushless double-rotor machine," *IEEE Transactions on Power Electronics*, Vol. 36, No. 1, 423–432, Jan. 2021.

[19] Zhao, Y., X. Ren, X. Fan, D. Li, and R. Qu, "A high power factor permanent magnet vernier machine with modular stator and yokeless rotor," *IEEE Transactions on Industrial Electronics*, Vol. 70, No. 7, 7141–7152, Jul. 2023.

[20] Yu, Y., Y. Pei, and F. Chai, "Power factor analysis in spoke-type permanent magnet vernier motors with different slot-pole combinations for in-wheel direct drive," *IEEE Transactions on Transportation Electrification*, Vol. 9, No. 1, 642–655, Mar. 2023.

[21] Zang, K., Y. Cai, J. Zhu, H. Liao, M. Li, and Q. Liu, "Optimized design of high power factor fault-tolerant permanent magnet vernier rim-driven machine," *Progress In Electromagnetics Research C*, Vol. 144, 75–83, 2024.